

FOUR NEW ECLIPSING MID M-DWARF SYSTEMS FROM THE NEW LUYTEN TWO TENTHS CATALOG

JONATHAN M. IRWIN, DAVID CHARBONNEAU, GILBERT A. ESQUERDO, DAVID W. LATHAM, JENNIFER G. WINTERS
Harvard-Smithsonian Center for Astrophysics, 60 Garden St., Cambridge, MA 02138, USA

JASON A. DITTMANN, ELISABETH R. NEWTON

Kavli Institute for Astrophysics and Space Research, Massachusetts Institute of Technology, 77 Massachusetts Avenue, Cambridge, MA 02139, USA

ZACHORY K. BERTA-THOMPSON

Department of Astrophysical and Planetary Sciences, University of Colorado, Boulder, CO 80309, USA

PERRY BERLIND AND MICHAEL L. CALKINS

Fred Lawrence Whipple Observatory, Smithsonian Astrophysical Observatory, 670 Mount Hopkins Road, Amado, AZ 85645, USA
Draft version August 10, 2018

ABSTRACT

Using data from the M_{Earth}-North and M_{Earth}-South transit surveys, we present the detection of eclipses in four mid M-dwarf systems: LP 107-25, LP 261-75, LP 796-24, and LP 991-15. Combining the M_{Earth} photometry with spectroscopic follow-up observations, we show that LP 107-25 and LP 796-24 are short-period (1.388 and 0.523 day, respectively) eclipsing binaries in triple-lined systems with substantial third light contamination from distant companions. LP 261-75 is a short-period (1.882 day) single-lined system consisting of a mid M-dwarf eclipsed by a probable brown dwarf secondary, with another distant visual brown dwarf companion. LP 991-15 is a long-period (29.3 day) double-lined eclipsing binary on an eccentric orbit with a geometry which produces only primary eclipses. A spectroscopic orbit is given for LP 991-15, and initial orbits for LP 107-25 and LP 261-75.

Subject headings: stars: binaries: eclipsing – stars: low-mass, brown dwarfs

1. INTRODUCTION

Eclipsing binaries are important astrophysical tools because they are able to provide largely model-independent, precise measurements of stellar masses and radii. Observations of the best-characterized examples reveal a systematic tendency of theoretical stellar evolution models to underpredict the radii of main sequence stars with convective outer envelopes (e.g., Andersen 1991; Torres et al. 2010).

Due to the special geometric configuration required for a spectroscopic binary to eclipse, such systems are rare. Observations are particularly sparse for fully convective M-dwarfs (stars with masses below approximately $0.35 M_{\odot}$; e.g., Chabrier & Baraffe 1997), and while recent observational progress has begun to fill in the parameter space between $0.2 M_{\odot}$ and $0.35 M_{\odot}$, there are still very few systems containing components below $0.2 M_{\odot}$ with precisely measured parameters (e.g., Nefs et al. 2013; Dittmann et al. 2017).

We operate the M_{Earth} project, an all-sky survey using two robotic telescope arrays to search for transiting planets orbiting fully convective M-dwarfs within 33 pc by obtaining high-cadence time series differential photometry (Nutzman & Charbonneau 2008). This survey is also highly sensitive to eclipsing binaries, which present much larger photometric signal sizes than transiting planets, and has been optimized for efficient recovery of objects with long orbital periods.

In previous papers, we have presented three eclipsing stellar systems (Irwin et al. 2009, 2011b; Dittmann et al.

2017) and one brown dwarf system (Irwin et al. 2010) detected with M_{Earth}. This paper presents details of four additional eclipsing systems detected over the same time period. Three are stellar systems (LP 107-25, LP 796-24 and LP 991-15), for which we report initial observations and characterization, but several concerns must be addressed before masses and radii of the components can be determined at the level required to test stellar models. The fourth (LP 261-75) is a single-lined system with a probable brown dwarf companion.

2. TARGET SELECTION AND PROPERTIES

Target selection for M_{Earth}-North is described in detail in Nutzman & Charbonneau (2008), and for M_{Earth}-South in Irwin et al. (2015). All four targets presented here were selected for observation based on photometric distance estimates placing them within 33 pc, a volume limit inherited from the work of Lépine (2005), upon which our original target selection was based. These distances were underestimated in three cases due to these targets being unresolved multiples in the original photometry. Overluminosity results in a larger effective volume limit for such systems in M_{Earth} when using photometric distance estimates, enhancing the detection rate.

This factor combined with the greatly improved availability of astrometric parallaxes for the M_{Earth} sample in recent years, and the continuing demand to push to smaller planet sizes, has resulted in reprioritization of the M_{Earth} target list and elimination or deprioritization of the majority of these more distant sources. These

changes were implemented during the 2016–2017 period. While this is very beneficial for planet detection it has likely considerably impacted detection of new eclipsing binaries, so in this publication we provide details of the final accumulated set of systems detected prior to the completion of these changes which were not published individually.

In Table 1, we summarize the photometric and astrometric properties of the four systems gathered from the literature: right ascension and declination α , δ ; proper motions μ_α , μ_δ ; astrometric parallax π_{trig} ; GAIA G , G_{BP} and G_{RP} photometry; infrared magnitudes $J_{2\text{MASS}}$, $H_{2\text{MASS}}$, $K_{2\text{MASS}}$ from 2MASS (Skrutskie et al. 2006); and spectral type (where available). We use the identifiers given in the NLTT throughout this work, but for LP 107-25 this identifier does not appear to have been used previously in the literature, so we also provide 2MASS identifiers in the table as an alternative. GAIA parameters are from Data Release 2 (DR2), which was released during the final stages of preparation of the manuscript. We have updated the parallaxes, but the positions and proper motions given in the table are the original ones assumed during the analysis.

3. MEARTH PHOTOMETRIC OBSERVATIONS

The MEarth data themselves, data reduction, and analysis methods have been described in detail in previous papers (Irwin et al. 2011a,b; Berta et al. 2012; Newton et al. 2016). The objects presented here were detected during the 2011–2017 observing seasons, during which time the configuration of both instruments was relatively stable, with all observations taken using the same RG715 filter bandpass.

Eclipses in LP 107-25 were detected during a search for photometric rotation periods performed at the end of the 2011–2013 observing period on approximately weekly cadence data intended for astrometry. The other three systems were all detected by MEarth’s real-time trigger based on single events in 2014 June (LP 991-15), 2014 December (LP 796-24), and 2017 June (LP 261-75).

In all four cases, after the initial detection was made additional photometric observations were gathered for follow-up, both during the eclipse windows at high cadence using back-to-back exposures, and at our standard 30 minute cadence between eclipse windows to search for any out-of-eclipse variations. In these mid M-dwarf systems the out-of-eclipse variations are usually dominated by rotational modulation (presumed to be due to starspots) rather than effects intrinsic to close binary stars such as ellipsoidal variation or reflection, but are important for modeling.

MEarth light curves require some pre-processing to remove bad data prior to use. For this publication we simply filter out data points taken through heavy clouds by requiring the magnitude zero point for the image was no more than 0.5 mag higher than a running average, where this average was computed by outlier resistant fitting of straight line segments to the magnitude zero point as a function of time for images taken with a stable instrument configuration (the same “instrument version number” in the light curve table). We note that the throughput has evolved substantially over the time period of observations presented here and shows a large jump at the 2016 summer shutdown when the telescope

optics were cleaned, and we consider points taken before and after this time to be different instrument configurations for the purpose of this analysis. A few data points with large pointing errors due to target acquisition problems were also discarded. The light curve data are given in an electronic table. This table provides the original light curve data used as input to the models, so the corrections described in §6.6 have not been applied.

Finding charts for all four objects, showing the position and size of the MEarth photometric apertures as well as source proper motion using previous epochs of imaging, are shown in Figure 1. The MEarth aperture for LP 107-25 is contaminated by a fainter background source but apertures for the other targets appear to be clean to the limiting magnitude of the first epoch plate scans. LP 261-75 also has high-contrast imaging observations from Bryan et al. (2016) placing upper limits on the presence of visual companions at very small angular separations.

The photometric ephemerides, orbital parameters, and rotation periods for the targets are summarized in Table 2, where we use the final solutions presented in §6 and §7 but combine these parameters into a single table for convenience. The quantities given for each system are the epoch of inferior conjunction T_0 and orbital period P ; the epoch of superior conjunction T_{sec} for systems with secondary eclipses; and the photometric rotation period P_{rot} where this differs from the orbital period.

We note that our models have been adjusted for light travel time across the eclipsing system (in the solar system, this effect is called the Rømer delay). This correction is needed for precise observations of systems with two eclipses to avoid erroneously inferring small amounts of eccentricity ($e \cos \omega$) due to the displacement of the secondary eclipse time that results from this signal being emitted further away from the observer than the primary eclipse signal in systems where $q < 1$. The conjunction times T_0 and T_{sec} presented in the table are reckoned as if they were communicated to the observer by a light signal emitted from the barycenter of the eclipsing system. They are not eclipse times (as would be observed) where the eclipse signals originate from the position of the star closer to the observer. These corrections depend on the mass ratio and physical size of the system and are below 1 minute for all of the systems presented here, but may need to be applied for precise work.

In several objects the uncertainties on T_0 from the Monte Carlo procedure are very small. It is likely these have been underestimated due to correlated noise, which has not been taken into account in this analysis. The contribution of systematic error in the shutter timing also begins to become important at this level, and is not known to better than approximately 1 second.

4. SPECTROSCOPIC OBSERVATIONS

For the three systems readily accessible from the Northern hemisphere (LP 107-25, LP 261-75, and LP 796-24), spectroscopic observations were gathered using the Tillinghast Reflector Echelle Spectrograph (TRES) on the 1.5m Tillinghast reflector at Fred Lawrence Whipple Observatory (FLWO). Typical exposure times were $3 \times (900 - 1300)$ s per epoch using the medium fiber ($R \simeq 44000$) and were varied at the telescope depending on observing conditions.

TABLE 1
SUMMARY OF THE PHOTOMETRIC AND ASTROMETRIC PROPERTIES OF THE FOUR SYSTEMS.

Parameter	LP 107-25	LP 261-75	LP 796-24	LP 991-15
2MASS identifier	J21280940+6321013	J09510459+3558098	J13004029-2010434	J01234181-3833496
$\alpha_{\text{ICRS},2000.0}$	21:28:09.40	09:51:04.58	13:00:40.26	01:23:41.84
$\delta_{\text{ICRS},2000.0}$	+63:21:01.4	+35:58:09.5	-20:10:43.8	-38:33:49.6
μ_{α} (arcsec/yr)	0.036 ± 0.008	-0.106 ± 0.008	-0.292 ± 0.002	0.243
μ_{δ} (arcsec/yr)	0.189 ± 0.008	-0.171 ± 0.008	-0.156 ± 0.002	0.000
Source	1	1	2	2MASS/NLTT
π_{trig} (arcsec)	0.021033 ± 0.000094	0.02945 ± 0.00014	0.02529 ± 0.00012	0.031633 ± 0.000064
G	12.749	13.833	13.980	13.736
G_{BP}	14.163	15.635	15.840	15.541
G_{RP}	11.586	12.541	12.692	12.455
Source	3	3	3	3
$J_{2\text{MASS}}$	9.988 ± 0.024	10.577 ± 0.021	10.814 ± 0.022	10.620 ± 0.026
$H_{2\text{MASS}}$	9.406 ± 0.028	9.960 ± 0.019	10.205 ± 0.025	10.059 ± 0.024
$K_{2\text{MASS}}$	9.164 ± 0.022	9.690 ± 0.019	9.918 ± 0.021	9.749 ± 0.023
Spectral type	...	M4.5	M4.5	M4.5
Source	...	4	5	5

REFERENCES. — (1) Lépine & Shara (2005), (2) Altmann et al. (2017), (3) Gaia Collaboration et al. (2018a), (4) Reid & Walkowicz (2006), (5) Reid et al. (2003).

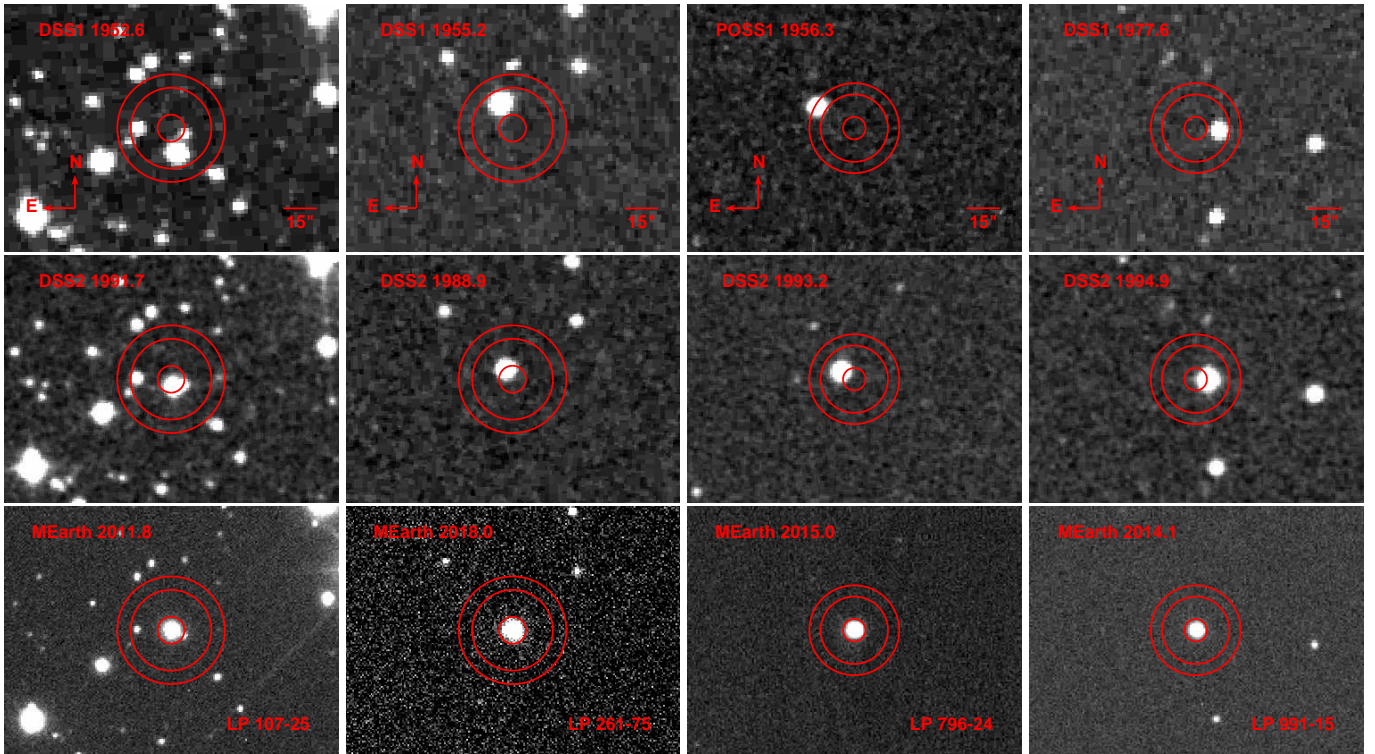


FIG. 1.— Finding charts showing data from the first and second epoch Digitized Sky Survey (with the exception of LP 796-24, where the first epoch is the SuperCOSMOS scan of the POSS-I “red” plate; Hambly et al. 2001) and the MEarth master image, in time order from top to bottom. The circles show the approximate position and size of the photometric aperture and sky annulus used to produce light curves from the MEarth images. All of the panels have the same orientation and scale on sky, the differences in size of the aperture and sky annulus are due the use of a different types of CCDs for MEarth-North and MEarth-South, which have different pixel sizes.

TABLE 2
PHOTOMETRIC EPHEMERIDES, ECCENTRICITY AND ROTATION FOR THE FOUR SYSTEMS.

Parameter	LP 107-25	LP 261-75	LP 796-24	LP 991-15
T_0 (BJD-TDB)	2456570.714584 ± 0.000036	2458159.731511 ± 0.000020	2457016.818868 ± 0.000015	2457269.890136 ± 0.000032
P (days)	1.388417440 ± 0.000000074	1.8817205 ± 0.0000011	0.523438589 ± 0.000000014	29.2678016 ± 0.0000081
T_{sec} (BJD-TDB)	2456571.407410 ± 0.000069	...	2457017.080587 ± 0.000015	...
Eclipse geometry	total	total	grazing	grazing
P_{rot} (days)	synchronized	2.22	synchronized	34

NOTE. — We refer the reader to Irwin et al. (2011a) for a discussion of the uncertainties in rotation periods derived from MEarth data.

LP 991-15 is also accessible with TRES, but only at high airmass and for a limited amount of time per night. Due to the anticipated need for a large number of long exposures on this system to measure the spectroscopic orbit, we opted instead to use the CHIRON instrument on the SMARTS 1.5m telescope at Cerro Tololo Inter-American Observatory (CTIO). Typical exposure times were 3×1200 s per epoch in fiber mode ($R \simeq 25\,000$).

These spectrographs are quite similar, so the remainder of the discussion has been combined and is presented in parallel for both instruments.

ThAr frames were taken before and after each set of exposures and used for wavelength calibration. This is standard operating procedure for TRES but should be explicitly requested for CHIRON. Data were reduced using the standard reduction pipelines provided for both instruments (Buchhave et al. 2010; Tokovinin et al. 2013).

The extracted spectra were not blaze corrected to preserve the photon weighting in the cross-correlations, but the blaze function derived from the flat fields was retained for later use. We note that the extracted spectra are not sky subtracted for either instrument, and in the case of CHIRON the instrumental background also appears to not be removed and adds substantially to the counts seen in the extracted spectra, particularly for long exposures. The residual instrumental background is successfully removed by our standard background subtraction prior to cross-correlation, for which we use quartic Legendre polynomials. In order to prevent contamination from sky emission lines or cosmic ray hits, we reject emission features using 5σ clipping prior to cross-correlation.

Observed template spectra were obtained for use in the cross-correlation analysis. For both instruments these were high signal to noise ratio spectra of Barnard’s Star (Gl 699), obtained on UT 2011 April 15 for TRES and UT 2014 September 18 for CHIRON. Following our earlier work we adopt a Barycentric radial velocity of -110.3 ± 0.5 km s $^{-1}$ for Barnard’s Star, where the stated uncertainty reflects our estimate of the systematic error. We note that this velocity zero point error propagates to all “absolute” Barycentric velocities given in this paper, and in particular it usually dominates the final uncertainty in the γ velocity. In the tables we have given only the random error from the Monte Carlo analysis, but note that for most applications this should be combined with the systematic error in the velocity zero point.

For cross-correlation analysis to determine radial velocities, we use a single order of the spectrum close to 7100Å dominated by strong molecular features (mostly due to TiO). For TRES this is the 41st order in the extracted spectrum file (numbering from 1 for the bluest extracted order), where we use a wavelength range of 7065–7165Å. This range removes part of the red end of the order, which is contaminated by telluric absorption features. For CHIRON we use the 46th extracted order with a wavelength range of 7040–7120Å. The signal to noise ratios of the target star spectra were approximately 10–30 per pixel in this wavelength range (the pixel scale is 0.06Å/pix for TRES and 0.10Å/pix for CHIRON) except for LP 796-24 which had a signal to noise ratio of approximately 5 per pixel.

5. SPECTROSCOPIC ANALYSIS

Our initial “reconnaissance” procedure for suspected spectroscopic binaries is as follows. We aim to obtain exposures at one or both quadratures (as estimated from the photometric ephemeris, assuming a circular orbit as necessary in systems with only a single eclipse) in order to maximize separation of the spectral lines in systems with composite spectra. These are analyzed using standard cross-correlation procedures (Kurtz & Mink 1998). We also use least-squares deconvolution (LSD; Donati et al. 1997) for visualization purposes, which gives higher velocity resolution for very closely separated lines at the cost of being more sensitive to noise.

All four systems have H α emission, and in cases where this emission is strong the emission line can have a much higher signal to noise ratio than the surrounding continuum or the regions used for the LSD, so this feature is also examined. It should be noted that these emission lines have an intrinsically broad line profile with a non-Gaussian form and originate in the chromosphere so are not necessarily at precisely the same radial velocity as the photosphere. Our spectra were extracted using cosmic ray rejection, which is known to affect strong emission features, and are neither flux calibrated nor background subtracted, so we do not attempt to provide quantitative measurements of this emission feature. The H α region in particular is contaminated by uncorrected sky emission lines in both instruments, in addition to the large additive instrumental background in the case of the CHIRON observations.

The appropriate method for extraction of radial velocities depends on the number of spectroscopic components found. We now discuss the systems in order of increasing complexity (number of components). The radial velocities are given in Table 3. We use the symbols v_j for the radial velocity of star j and h for the cross-correlation at the best-fitting radial velocity (normalized to unity) throughout this section.

5.1. Single-lined system (LP 261-75)

LP 261-75 was found to be single-lined, with some rotational broadening. Radial velocities were obtained from 8 epochs using standard cross-correlation analysis with rotational broadening applied to the template spectrum immediately prior to correlation. The appropriate amount of rotational broadening¹ v_{b1} was determined by searching for maximum peak correlation as a function of v_{b1} for each epoch individually, adopting the mean value of $v_{b1} = 7.57 \pm 0.10$ km s $^{-1}$ (where the stated uncertainty is the empirical standard error in the mean calculated from the sample of 8 measurements) for the final analysis of all the epochs.

We note that this value of v_{b1} is only barely above the spectral resolution, and could be influenced by other sources of broadening than rotation. The treatment of rotational broadening in the analysis is based on sampling the spectrum in $\log \lambda$ at approximately 1/32 pixel and neglects any rotational broadening which might be

¹ Where we denote the rotational broadening applied to star j as v_{bj} . We make an explicit distinction between *assumed* or *adopted* broadening in the correlation analysis using this symbol and *true* rotational broadening $v_{rot} \sin i$, which is not necessarily the same, as discussed in the text.

TABLE 3
RADIAL VELOCITY DATA.

BJD-TDB (days)	v_1 (km/s)	v_2 (km/s)	v_3 (km/s)	h	t_{exp} (s)
LP 107-25 ($\alpha = 0.0748$, $\beta = 0.2048$, $v_{b1}, v_{b2} = 15.5, 6.7$ km/s)					
2456560.6761	33.524	-124.200	-9.361	0.9435	2700
2456573.7180	-40.958	94.424	-14.312	0.8713	2700
2456574.7155	22.625	-87.527	-14.641	0.9280	2700
2456575.7592	25.449	-90.200	-14.774	0.8971	3600
2456576.7053	-43.197	103.919	-15.159	0.9227	3000
2456578.6669	35.967	-121.785	-16.004	0.9327	2700
2457583.9030	38.591	-119.870	-22.153	0.8683	3000
LP 261-75 ($v_{b1} = 7.57$ km/s)					
2458082.9421	-25.724	0.8750	3600
2458083.9371	16.321	0.8922	3600
2458107.0107	-2.686	0.8374	3600
2458107.9946	-4.583	0.8233	3600
2458119.0290	-21.240	0.8719	3900
2458119.9922	9.527	0.8693	3900
2458172.8909	-4.056	0.8448	3600
2458187.7043	11.282	0.8778	3600
LP 991-15 ($\alpha = 0.6510$)					
2456948.5523	-2.879	22.267	...	0.8910	3600
2456951.5435	-16.642	38.432	...	0.8927	3600
2456954.5368	-9.545	30.287	...	0.9188	3600
2456955.5368	-7.524	27.199	...	0.9146	3600
2456957.6848	-2.192	21.981	...	0.8679	3600
2456965.5309	14.733	1.205	...	0.9219	3600
2456972.6082	32.169	-18.928	...	0.9240	3600
2456976.6687	19.769	-4.407	...	0.8909	3600
2456978.6783	-13.175	34.477	...	0.8927	3600
2456996.5986	18.827	-2.756	...	0.8650	3600
2456998.5887	23.689	-8.781	...	0.8838	3600
2457002.5769	33.801	-20.652	...	0.9027	3600
2457003.6872	35.629	-22.681	...	0.8976	3600
2457004.6962	33.558	-20.900	...	0.9022	3600
2457005.5698	25.569	-10.817	...	0.8625	3600
2457008.6712	-16.636	39.062	...	0.8931	3600
2457009.5970	-17.367	39.107	...	0.9097	3600
2457010.6070	-15.547	37.708	...	0.9167	3600
2457013.5569	-8.348	28.807	...	0.9092	3600
2457014.5480	-6.102	25.704	...	0.8468	3600
2457015.5512	-3.587	23.314	...	0.8868	3600
2457016.5503	-1.238	20.438	...	0.9020	3600
2457017.6878	1.135	17.841	...	0.8831	3600
2457018.5646	3.278	15.746	...	0.8702	3600
2457031.6008	33.469	-20.823	...	0.8781	3600
2457032.6102	35.108	-22.568	...	0.8943	3600
2457033.5890	35.156	-22.029	...	0.9177	3600
2457047.5634	2.372	15.914	...	0.9201	3600
2457180.8935	29.556	-15.840	...	0.8678	3600
2457182.8806	-5.700	26.214	...	0.8342	3600

present in the template spectrum, so it is only approximate for small v_{b1} and could potentially also impact the results. This should therefore not be treated as a measurement of the rotational broadening.

Radial velocity uncertainties were derived from the scatter in the residuals during fitting and were approximately 0.14 km s^{-1} for this system.

5.2. Double-lined system (LP 991-15)

LP 991-15 was observed after only a single eclipse had been detected, so the orbital period was unknown and it was not possible to arrange to take data at the optimum orbital phase. After obtaining several epochs with insufficient velocity separation between the components we eventually determined this object to be double-lined, with negligible rotational broadening, and obtained a total of 38 epochs. Radial velocities were derived using TODCOR (Zucker & Mazeh 1994), following the proce-

dures in Irwin et al. (2011b). Eight epochs with velocity separation $|v_1 - v_2| < 10 \text{ km s}^{-1}$ were discarded, leaving 30 epochs for the final analysis. The spectroscopic light ratio α was derived by searching for the maximum sum of the squares of the peak correlation over all the remaining epochs, and gave $\alpha = 0.6510$. The radial velocity uncertainties derived during fitting were approximately 0.16 km s^{-1} for the primary and 0.31 km s^{-1} for the secondary.

5.3. Triple-lined systems (LP 107-25 and LP 796-24)

LP 107-25 and LP 796-24 were both found to be triple-lined with distant, slowly rotating companions, and an inner, rapidly rotating eclipsing binary pair. Throughout the discussion of these objects, we refer to the eclipsing binary pair as the “primary” and “secondary”, and the third star as the “tertiary”, with respective indices 1, 2 and 3, even though in the case of LP 796-24 it is possible the star we refer to as the “tertiary” is the most massive.

Radial velocities for these triple-lined systems were derived using TRICOR (Zucker et al. 1995), which is the extension of the TODCOR method to three dimensions. This requires three template spectra and two light ratio parameters α and β . In the present case all three templates were the same spectrum of Barnard’s Star but were allowed to have different amounts of rotational broadening. As for the analysis of LP 991-15, two epochs for LP 107-25 with velocity separation $|v_1 - v_2| < 10 \text{ km s}^{-1}$ were discarded.

In both objects star 3 was found to have negligible rotational broadening, so none was applied to the template, and stars 1 and 2 were found to be rotating synchronously within the uncertainties, so the v_b values for these stars were fixed to the values calculated from the models presented in the following sections, leaving only the two parameters α and β to be determined using TRICOR.

For LP 107-25, the velocity uncertainties derived during fitting were approximately 1.6 km s^{-1} for the primary and tertiary, and 2.5 km s^{-1} for the fainter secondary.

For LP 796-24, we only obtained 3 usable epochs with low signal to noise ratios, which yielded unusually low peak correlation. The velocities and light ratios do not seem to be reliably determined. We therefore do not present them in the table, and due to the lack of spectroscopic information needed for a full solution of this system, we only present the ephemeris and show the MEarth light curve in this paper.

6. MODELS

We use a simplified version of the procedure described in Irwin et al. (2011b) to model the light curves and radial velocities simultaneously for the multiple-lined systems, which is based on the Nelson-Davis-Etzel model (Nelson & Davis 1972; Etzel 1981; Popper & Etzel 1981) and its descendant JKTEBOP (Southworth et al. 2004a,b). Since the Irwin et al. (2011b) publication, the light curve generator was rewritten², and now uses the analytic method of Mandel & Agol (2002) to perform the eclipse calculations. This model is physically equivalent but avoids the

² This software is available online at the following URL: <https://github.com/mdwarfgeek/eb>

trade-off between performance and accuracy inherent in the original implementation (due to use of numerical integration).

Table 4 summarizes the parameters in the models and their symbols used in the text and tables, and Table 5 gives the values adopted for each system (excluding LP 796-24, where we did not undertake a full solution). We refer the reader to Irwin et al. (2011b) for a discussion of the choice of priors for these parameters, which have been adopted here except as noted in the text. The values of the modified Jeffreys prior parameter K_a used in the radial velocity analysis were set to 10% of the s_j parameters for the radial velocities.

Similar to our analysis of other single-lined systems (e.g., Irwin et al. 2010 and the M_{Earth} transiting planets) a light curve model with a completely dark secondary was used for LP 261-75, with the photometric ephemeris imposed on the radial velocity solution using priors for simplicity given that the solution of such systems is essentially separable. This used the same underlying model as for the multiple-lined systems, but neglecting ellipsoidal variation and light travel time (due to lack of knowledge of the radial velocity semiamplitude of the secondary), the reflection effect, and gravity darkening. The radial velocity model fitting for this single-lined system was done using the same implementation as Winters et al. (2018) with priors as described there.

In the following subsections we highlight several points of note specific to the present analysis.

6.1. Limb darkening and gravity darkening

Our photometry was all gathered using M_{Earth}, which was changed to a non-standard filter bandpass during the 2011 summer shutdown and used for all data analyzed here, so limb darkening coefficients now require more careful treatment. In addition, as discussed by Torres et al. (2017), gravity darkening coefficients are needed.

To allow the use of limb darkening and gravity darkening coefficients from standard tabulations, transformation equations were derived from the Sloan Digital Sky Survey i and z filters to M_{Earth}. These calculations were performed with the Limb Darkening Toolkit (LDTK; Parviainen & Aigrain 2015) using PHOENIX model atmospheres from Husser et al. (2013) and the M_{Earth} transmission function from Dittmann et al. (2016). We use the quadratic limb darkening law throughout the calculations.

Over the appropriate range of spectral type needed in this work, the following equation was found to be sufficient:

$$u(\text{MEarth}) = [2u(i) + 3u(z)] / 5 \quad (1)$$

where $u(\text{passband})$ refers to the limb darkening coefficient in each passband, and the transformation equation is the same for the linear and quadratic coefficients, which we denote as u and u' in this work due to use of the usual symbols for other purposes. We further assume that the same transformation applies to the gravity darkening coefficients.

Limb darkening coefficients were adopted from the tables of Claret et al. (2012), using fixed values of $\log g = 5.0$, and the least-squares method, and interpolated in effective temperature T_{eff} . Gravity darkening coefficients

were adopted from Claret & Bloemen (2011) using the same value of $\log g$ and PHOENIX atmosphere models but interpolated in the native $\log T_{\text{eff}}$ abscissa used in the table. These tables give the quantity $y(\lambda)\beta$ in the notation of Torres et al. (2017) needed as input to the light curve model directly (we note that the definition of the symbol y used in Claret & Bloemen 2011 differs from the definition we and Torres et al. 2017 use).

Effective temperatures are not well-constrained for any of our targets, so we use the tables of Pecaut & Mamajek (2013) for main sequence stars³ to estimate T_{eff} with linear interpolation. For the multiple-lined systems LP 107-25 and LP 991-15 we interpolate using the measured component masses. For the single-lined system LP 261-75 we use the spectral type given in Table 1. The adopted values for all four objects are given in Table 5. Precision in excess of 50 K is not warranted, especially given the intrinsic scatter and propensity for systematic error in effective temperature scales for M-dwarfs, so the T_{eff} values were rounded to the nearest 50 K.

6.2. Third light

Two of our systems (LP 107-25 and LP 796-24) have a large amount of third light, which dilutes the measured eclipse depths and must be accounted for in the light curve solutions. The determination of this quantity from otherwise unconstrained light curve models is a notoriously degenerate problem (e.g., Nelson & Davis 1972) and it is likely our ground-based light curves lack the precision required to attempt this.

In order to make progress, we use the spectroscopic measurements. The quantity required as input to the model is the third light divided by total light in the observed photometric bandpass, which we denote as L_3/L_{tot} where L_j is the light of the j th star, in arbitrary units, and $L_{\text{tot}} = L_1 + L_2 + L_3$. The TRICOR solutions provide two light ratios $\alpha \simeq L_2/L_1$ and $\beta \simeq L_3/L_1$ where the approximations serve to emphasize the assumption that the effective bandpass of the spectroscopic measurement matches that of the photometry. This is not the case, so the resulting value of the third light parameter inherits an uncertainty from this procedure which we discuss in more detail in §7.1. We apply this constraint using a Gaussian prior, adopting a standard deviation of 0.05.

The LP 261-75 and LP 991-15 systems do not show any evidence of third light in the spectroscopy or in imaging observations, so we adopt a fixed value of $L_3 = 0$.

6.3. Light ratios

As discussed in Irwin et al. (2011b), in most grazing configurations it is also necessary to impose a spectroscopic constraint on the light ratio L_2/L_1 using the TODCOR (or TRICOR) α parameter when working with ground-based light curves.

In the case of LP 261-75 there is no evidence for light from the secondary in the light curves or spectra so this was fixed to zero, which is equivalent to fixing $J = 0$. The eclipse is total so the light curves are then sufficient to constrain all three geometric parameters R_2/R_1 , $\cos i$, and $(R_1 + R_2)/a$.

³ From http://www.pas.rochester.edu/~emamajek/EEM_dwarf_UBVIJHK_colors_Teff.txt version 2017.10.19.

TABLE 4
DEFINITION OF PARAMETERS USED IN THE MODELS.

Parameter	Description
J	Central surface brightness ratio (secondary / primary) in MEarth.
$(R_1 + R_2)/a$	Sum of the component radii R_1 and R_2 divided by semimajor axis a .
R_2/R_1	Radius ratio.
$\cos i$	Cosine of orbital inclination i .
$e \cos \omega$	Eccentricity e multiplied by cosine of argument of periastron ω .
$e \sin \omega$	Eccentricity multiplied by sine of argument of periastron.
u_1	Linear limb darkening coefficient for primary.
u'_1	Quadratic limb darkening coefficient for primary.
u_2	Linear limb darkening coefficient for secondary.
u'_2	Quadratic limb darkening coefficient for secondary.
$(y\beta)_1$	Product of gravity darkening coefficient and exponent for primary.
$(y\beta)_2$	Product of gravity darkening coefficient and exponent for secondary.
A_1	Albedo of primary.
A_2	Albedo of secondary.
L_2/L_1	Light ratio (secondary/primary).
L_3/L_{tot}	Third light divided by total system light.
F_1	Rotation parameter of primary (orbital period / rotation period).
a_{11}	Primary out-of-eclipse sine coefficient for fundamental.
b_{11}	Primary out-of-eclipse cosine coefficient for fundamental.
a_{12}	Primary out-of-eclipse sine coefficient for 2nd harmonic.
b_{12}	Primary out-of-eclipse cosine coefficient for 2nd harmonic.
K_1	Radial velocity semiamplitude of primary (for SB1s).
q	Mass ratio, M_2/M_1 .
$K_1 + K_2$	Sum of radial velocity semiamplitudes (for SB2s).
γ	Systemic radial velocity.
P	Orbital period.
T_0	Epoch of inferior conjunction.
z_j	Magnitude zero point for light curve segment j (see §6.6).
s_j	For light curves, error scaling factor for light curve j . For radial velocities, this parameter sets the adopted radial velocity uncertainty according to $\sigma_{ij} = s_j/h_i$ for data point i of star j , where h_i is the peak normalized cross-correlation from Table 3.
C	Common mode coefficient (described in §6.6).

NOTE. — This table updates Table 5 from Irwin et al. (2011b). We have changed some of the symbols and amended the descriptions following changes to the software, but the parameter set is reproduced here in full for convenience.

In LP 107-25 and LP 991-15, we apply the spectroscopic constraint using a Gaussian prior with a mean given by the spectroscopic value and a standard deviation of 0.05. It serves different roles in each object due to their configurations. In LP 107-25, due to the totally eclipsing geometry this constraint merely serves to supplement the information provided by the third light constraint. For LP 991-15, the spectroscopic constraint supplies essentially all of the information on the combination of J and R_2/R_1 in this system due to the grazing geometry combined with the lack of secondary eclipses.

6.4. Radius ratio

In LP 991-15, we need an additional constraint due to the lack of secondary eclipses, which would usually serve to constrain the parameter J (this is essentially determined by the relative depths of the primary and secondary eclipses and the adopted limb darkening law).

To make progress in this system, we use the empirical mass-radius relation of Bayless & Orosz (2006) to calculate the radius ratio from the measured component masses, and impose this as a Gaussian prior on R_2/R_1 .

We adopt a standard deviation of 0.05 on this radius ratio, based on the observed dispersion in the mass-radius relation. It is important to note that the results depend on the adopted mass-radius relation, the implications of which are discussed in §7.5.

6.5. Spots

All four systems show evidence of spots. The solutions in this work are preliminary in nature, so we have not undertaken a detailed treatment of the effect of these spots on the derived parameters. Instead, we simply adopt a standard “non-eclipsed spots” model in the terminology of Irwin et al. (2011b), placing the spots on the primary star. In the case of LP 107-25 and LP 261-75 it is unlikely the spots responsible for the modulations could be on any other component due to the large light ratios (and for LP 107-25 and LP 796-24 the synchronous rotation periods argue against the origin of the modulations being the tertiary, which has no rotational broadening in the spectroscopy for either object), but we have not attempted to allow for the effect of spot latitude (relative to the eclipse chord) by varying the “fraction of eclipsed

TABLE 5
ADOPTED PARAMETERS FOR EACH SYSTEM.

Parameter	LP 107-25	LP 261-75	LP 991-15
J	varied	0	varied
$(R_1 + R_2)/a$	varied	varied	varied
R_2/R_1	varied	varied	0.871 ± 0.050
$\cos i$	varied	varied	varied
$e \cos \omega$	varied	0	varied
$e \sin \omega$	varied	0	varied
$T_{\text{eff}1}$ (K)	3500	3100	3150
$T_{\text{eff}2}$ (K)	3050	...	3050
u_1	0.1857	0.2352	0.2269
u_1'	0.3205	0.4008	0.3932
u_2	0.2856	0	0.2856
u_2'	0.4549	0	0.4549
$(y\beta)_1$	0.2478	0	0.2978
$(y\beta)_2$	0.3203	0	0.3203
A_1	0.4	0	0.4
A_2	0.4	0	0.4
L_2/L_1	0.075 ± 0.050	0	0.651 ± 0.050
L_3/L_{tot}	0.160 ± 0.050	0	0
F_1	1.0	varied	varied
a_{11}	varied	varied	varied
b_{11}	varied	varied	varied
a_{12}	0	varied	0
b_{12}	0	varied	0
K_1	...	varied	...
q	varied	...	varied
$K_1 + K_2$	varied	...	varied
γ	varied	varied	varied
P	varied	varied	varied
T_0	varied	varied	varied

NOTE. — In this table, values without uncertainties indicate the parameter was fixed at this value, and values with uncertainties indicate the parameter was varied subject to a Gaussian prior with the mean and standard deviation given. The effective temperatures given are the values assumed when interpolating limb darkening and gravity darkening coefficients.

spots” parameter.

We caution that a more detailed treatment of the effect of spots would be necessary in any possible future use of these systems to derive precise estimates of light curve parameters and stellar radii.

6.6. Light curve nuisance parameters

Light curves from MEarth require correction for magnitude zero point offsets (predominantly thought to be caused by flat fielding error) when the target crosses the meridian and also when the instrument is removed from the telescope for servicing. In the light curves each place where a new magnitude zero point is needed is given a unique integer “segment number”, and we use these to apply the correction, adding a new free parameter z_j to the model for the magnitude zero point in each “segment” j appearing in each light curve.

We also inflate the observational uncertainties by adding error scaling parameters s_l for each light curve l (in the electronic table provided with the manuscript, these are identified by different “dataset names” in the second column). In the case of LP 261-75, the datasets

observed using different telescopes on the same night were combined for this purpose so we use one s parameter per night rather than the usual practice which would have assigned separate parameters to each telescope. LP 991-15 was observed in a similar fashion on two nights but these were found to benefit from being left with separate s_l coefficients due to tracking problems on specific telescopes.

Variations in atmospheric water vapor also introduce systematic variations in the MEarth photometry. This effect has been discussed in detail elsewhere (e.g., Irwin et al. 2011a; Newton et al. 2016). The photometric corrections are derived by averaging the light curves of all M-dwarfs observed at a given time from telescopes at the same site to produce a “common mode” light curve. In order to average as many target stars as possible this must be done in bins of roughly the standard observational cadence, which are 0.02 days. We find this sampling is too coarse to reliably correct high-cadence followup light curves such as used during eclipse windows in the present work, and in some cases such as LP 261-75 multiple telescopes were used to observe the same target, which adversely impacts determination of the common mode itself. We therefore apply this correction only to long-term light curves with out-of-eclipse parts of the time series and not the individual eclipses observed for followup. We use the symbol C for the common mode coefficient, which should be the same for all telescopes observing the same target, so only one coefficient is needed.

6.7. Method of solution and uncertainties

Non-linear least-squares model fitting (using MPFIT; Markwardt 2009; or `leastsq` from `scipy.optimize` in the case of LP 261-75) was performed to initialize the parameters and covariance matrices prior to the final Monte Carlo simulations. These fits used iterative 5σ outlier rejection for the light curves, and the resulting clipped light curves were the ones used in the Monte Carlo simulations. These outliers are predominantly in the out-of-eclipse monitoring portions and usually correspond to bad images (e.g., pointing errors, tracking problems, or clouds) and occasional stellar flares. The appropriate value of σ was calculated using a robust median absolute deviation (MAD) estimator, scaled to the Gaussian equivalent rms (e.g., Hoaglin et al. 1983).

Parameters and uncertainties were estimated using Monte Carlo simulations. For the multiple-lined systems, we used the same Adaptive Metropolis method used in Irwin et al. (2011b), with chains run for 2×10^6 steps, discarding the first 50% of these to allow the chain to “burn in” before being used for parameter estimation. For LP 261-75 we used the `emcee` package (Foreman-Mackey et al. 2013) with 250 walkers each run for a burn in of 10^4 steps, followed by 2×10^4 steps used for parameter estimation (resulting in a total of 5×10^6 samples from the posterior probability density function). In this paper we report the median as the central value and the 68.3 percentile of the absolute deviation of the posterior samples about the median as the uncertainty. This change was made compared to our previous work to produce symmetric uncertainties and thereby simplify interpretation of the results.

7. DISCUSSION AND ORBITAL SOLUTIONS

In this section, we first discuss a difficulty common to several of the objects, and then present solutions and discussion for each of the four objects individually. We give the jump parameters used in the Monte Carlo simulations and any derived parameters such as masses which are determined robustly. Derived parameters which are not well-determined are not presented, and while we have given sufficient information to calculate these we caution against doing so given their uncertainties. Consequently we also do not present comparisons to theoretical models, which would be premature given the preliminary nature of the solutions.

7.1. Spectroscopic vs photometric light ratios

An important source of uncertainty, and potentially also systematic error, in the models of the multiple-lined systems presented here (LP 107-25 and LP 991-15) results from the need to compute light ratios appropriate for models of the MEarth photometry using quantities measured spectroscopically with the TODCOR or TRICOR α and β parameters.

These problems arise if the components of the multiple system are not spectroscopically identical. In such cases the α or β parameters then depend not only on the appropriate light ratio, but also on the degree to which the depths of the absorption lines resemble the ones in the template (in this case, Barnard’s Star). The addition of rotational broadening and the need to correct for differences between the spectroscopic and photometric bandpasses present further complications.

We conducted simulations using PHOENIX model atmospheres from Husser et al. (2013) to estimate the appropriate transformation between the measured spectroscopic ratios and light ratios in the MEarth bandpass. We find that these appear to depend strongly on metallicity in addition to effective temperature (we speculate that this may be due to the use of molecular absorption features, predominantly due to TiO, when computing the spectroscopic ratios). Given that neither of these quantities are well determined for our targets, we have not attempted to apply any corrections for the present analysis. Instead, we simply use the spectroscopic values without correction and adopt an uncertainty of ± 0.05 , which we find to be a reasonable approximation to the error introduced by not applying the corrections over realistic ranges in effective temperature and metallicity.

This strongly downweights the small value of α for LP 107-25, where we find the appropriate correction factor is ill-determined due to the large difference in stellar type between the primary and the secondary. In this system, the third light parameter appropriate for the light curve models is better determined by virtue of a smaller spectral mismatch between the tertiary and primary so is given more weight in the solution. The alternative assumption of a constant relative error in the light ratio would assign too much weight to ratios far from unity.

We caution that this procedure is still somewhat arbitrary and has an impact on the resulting uncertainties in the physical parameters of interest, which is clearly undesirable. At present, it is difficult to make further progress using the same method until effective temperatures and metallicities can be constrained observation-

TABLE 6
PARAMETERS AND UNCERTAINTIES FOR
LP 107-25.

Parameter	Value
Jump parameters	
J	0.5035 ± 0.0029
$(R_1 + R_2)/a$	0.13931 ± 0.00077
R_2/R_1	0.431 ± 0.012
$\cos i$	0.0202 ± 0.0062
$e \cos \omega$	-0.001564 ± 0.000081
$e \sin \omega$	0.0040 ± 0.0021
q	0.3529 ± 0.0075
a_{11}	-0.00111 ± 0.00016
b_{11}	-0.00348 ± 0.00023
$(K_1 + K_2)$ (km/s)	159.3 ± 1.3
γ (km/s)	-5.29 ± 0.54
C	0.557 ± 0.021
s_1 (km/s)	1.50 ± 0.45
s_2 (km/s)	2.26 ± 0.66
Derived parameters	
i (deg)	88.84 ± 0.36
M_1 (M_\odot)	0.430 ± 0.010
M_2 (M_\odot)	0.1518 ± 0.0046
$(R_1 + R_2)$ (R_\odot)	0.6092 ± 0.0061
R_1 (R_\odot)	0.4256 ± 0.0065
R_2 (R_\odot)	0.1836 ± 0.0031

ally for our targets, and even with this information the results would still depend on the model atmospheres. A possible solution to the latter problem would be to use multiple systems which are resolved both visually and spectroscopically to calibrate empirical relations between photometric and spectroscopic light ratios, but there are not currently enough examples of such objects known to attempt to derive these relations.

A potentially superior approach for the two triple systems with distant tertiaries (LP 107-25 and LP 796-24) may be to attempt to resolve the tertiary from the inner binary using imaging observations in order to measure $L_3/(L_1 + L_2)$ directly. Such observations are not currently available, and these systems are distant, resulting in small expected angular separations, but this may be a fruitful avenue for future work. Light curves obtained in the same bandpass as the imaging observations could then be analyzed by imposing the measured light ratios directly, without incurring transformation uncertainties.

7.2. LP 107-25

Figure 2 shows the light curve and radial velocities for this system, and Table 6 gives our preliminary orbital solution. There is a small displacement in the secondary eclipse timing, where the eclipse appears approximately two minutes early compared to the prediction for a circular orbit. We have allowed non-zero eccentricity in the solution to account for this, which appears predominantly as a non-zero value of $e \cos \omega$. The value of $e \sin \omega$ is consistent with zero within reasonable uncertainties, especially when accounting for the tendency of solutions with limited numbers of radial velocities to overfit this quantity. Consequently the argument of periastron ω is ill-determined and we do not provide individual values for e and ω in the table.

A background star is seen overlapping the MEarth photometric aperture in Figure 1. This is not the star responsible for the third light, and is not included in the TRES fiber, which has a smaller diameter than

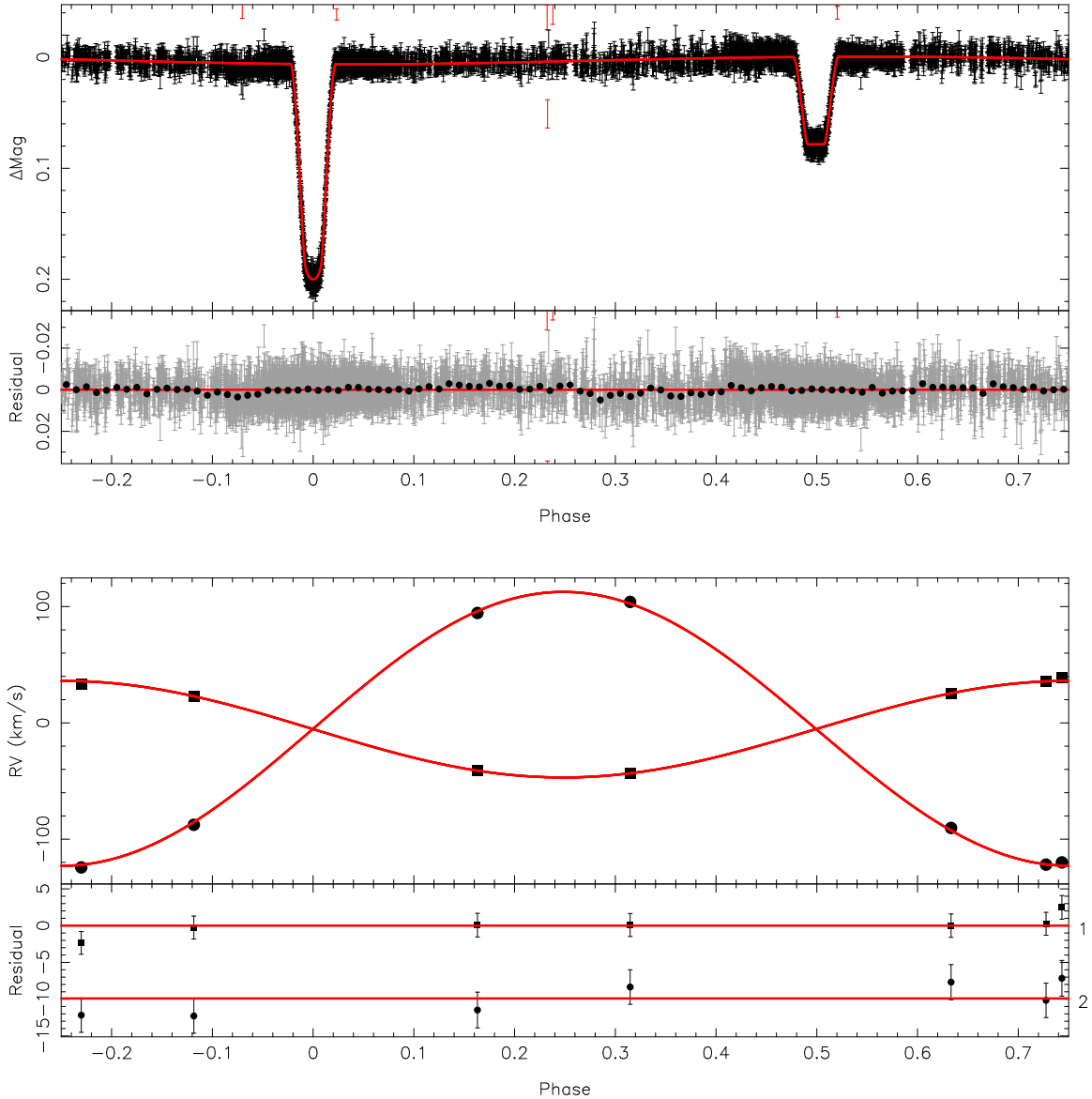


FIG. 2.— Top panels: phase-folded light curve for LP 107-25. Bottom panels: radial velocity curve. In each case there are two sub-panels, with the upper showing the data with the best fit overlaid, and the lower showing the residuals from the best fit. For the light curves, the magnitude zero point offsets and common mode have been removed to flatten the instrumental baseline, leaving only suspected astrophysical variations. Outliers rejected from the solution are shown in red. When plotting the residuals, the original data are shown in grey, and black points show the same data binned in phase into 100 equal size bins. For the radial velocities, square symbols show the velocities for the primary and filled circles for the secondary. The residuals for the two components are offset vertically for clarity.

the MEarth photometric aperture. This contaminating star is 4.72 magnitudes fainter than the target in the GAIA G_{RP} passband, and is bluer than the target in the $G_{\text{BP}} - G_{\text{RP}}$ color, so the contribution to the MEarth photometry should be negligible compared to the uncertainty inherited from the TRICOR-derived value of $\beta/(1+\alpha+\beta)$ for the brighter star that is the source of the third light in the spectroscopy.

We regard our solution as preliminary in both the masses, due to the limited number and quality of the radial velocities, and the possibility of a long-term trend due to the outer orbit; and in the radii due to the large amount of third light contamination. It is likely the uncertainties are underestimated as a result of these issues, and due to neglecting correlated noise in the analysis.

Comparison of these quantities to the predictions of theoretical models would therefore be premature, and we have not undertaken such an analysis at present.

7.3. LP 261-75

Table 7 gives our orbital solution for LP 261-75, and Figures 3 and 4 show this model overplotted on the data used in the analysis. We also observed several secondary eclipse windows which were not included in the models, but are shown in Figure 5 to justify the choice of fixing $J = 0$ in the solution.

We caution that the primary eclipse light curves show evidence of frequent spot crossings in the residuals, and the depths appear to be somewhat variable, meaning our nominal value for the radius ratio may exhibit system-

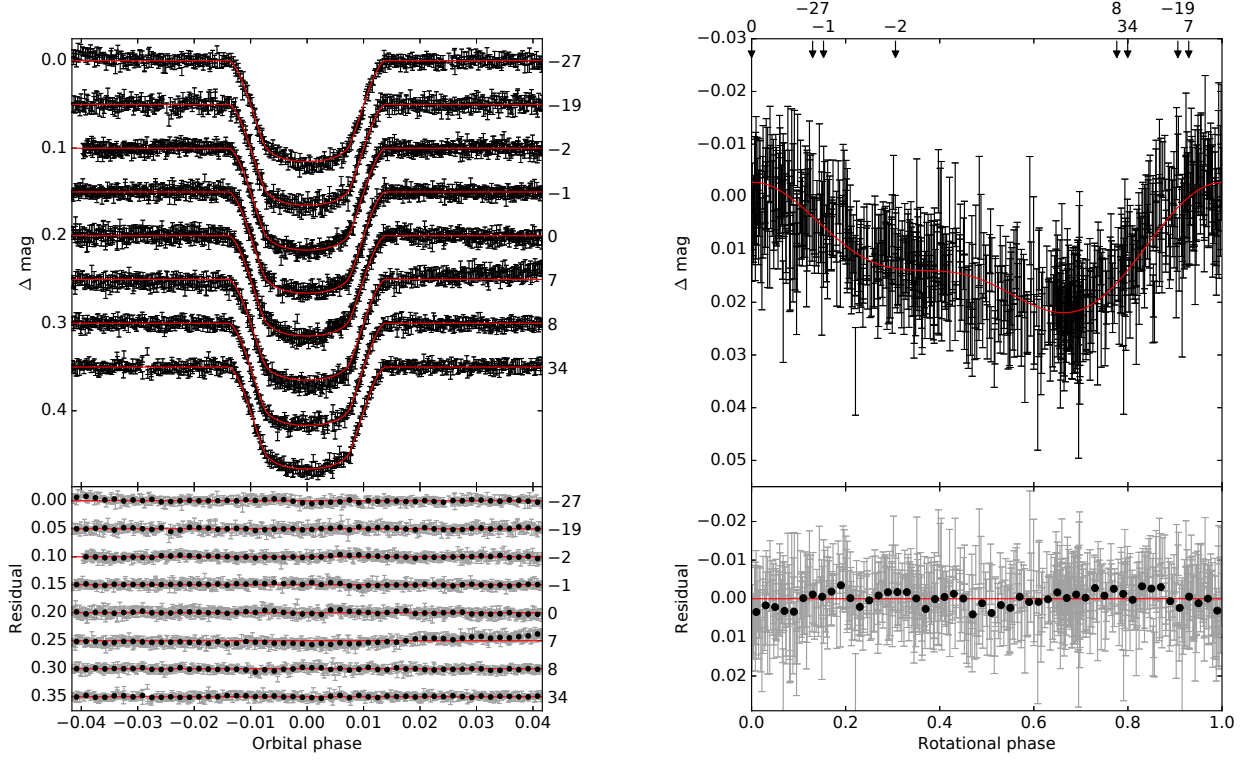


FIG. 3.— Light curves for LP 261-75 with the best fit overlaid. Left panels: primary eclipse windows with the out-of-eclipse modulation and magnitude zero point offsets removed to flatten the baseline. Different eclipses are offset vertically for clarity, and the cycle number (integer part of the normalized orbital phase) is given on the right. Right panels: out-of-eclipse modulation with the eclipse windows removed. Only the instrumental effects (magnitude zero point offsets and common mode) were corrected. The phases where eclipses were observed are indicated with arrows at the top of the diagram, giving the appropriate cycle numbers. When plotting the residuals, the original data are shown in grey, and black points show the same data binned in phase into 50 equal size bins.

TABLE 7
PARAMETERS AND UNCERTAINTIES FOR
LP 261-75.

Parameter	Value
Light curve jump parameters	
R_2/R_1	0.29484 ± 0.00034
$(R_1 + R_2)/a$	0.08843 ± 0.00035
$\cos i$	0.0152 ± 0.0011
F_1	0.84704 ± 0.00019
a_{11}	0.00299 ± 0.00025
b_{11}	0.00866 ± 0.00025
a_{12}	-0.00125 ± 0.00019
b_{12}	0.00396 ± 0.00021
C	0.787 ± 0.069
Radial velocity jump parameters	
γ (km/s)	-5.193 ± 0.054
K_1 (km/s)	21.942 ± 0.081
s_1 (km/s)	0.125 ± 0.037
Derived parameters (MLR-independent)	
i (deg)	89.131 ± 0.065
e (95% credible)	< 0.007
$f_1(M)$ (M_\odot)	0.002060 ± 0.000023
Derived parameters (MLR-dependent)	
q	0.2166 ± 0.0041
M_1 (M_\odot)	0.300 ± 0.015
M_2 (M_\odot)	0.0650 ± 0.0020
R_1 (R_\odot)	0.3131 ± 0.0049
R_2 (R_\odot)	0.0923 ± 0.0015
$v_{\text{rot},1}$ (km/s)	7.13 ± 0.11

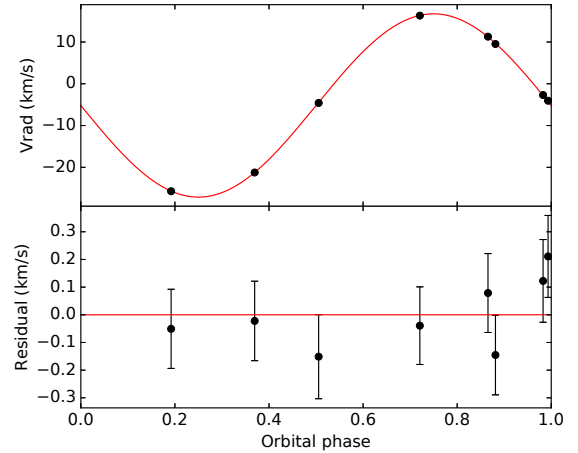


FIG. 4.— Single-lined radial velocity orbit for LP 261-75 with the best fit overlaid (top) and residuals (bottom).

atic errors depending on the distribution of spots on the stellar photosphere. The stellar spin and orbital period are not synchronized, which provides some information on the influence of the asymmetric component of the spot distribution (e.g., as discussed in Irwin et al. 2011b) but the number of eclipses available at present is rather limited so we have not attempted such an analysis.

Additional trial solutions were run allowing a different

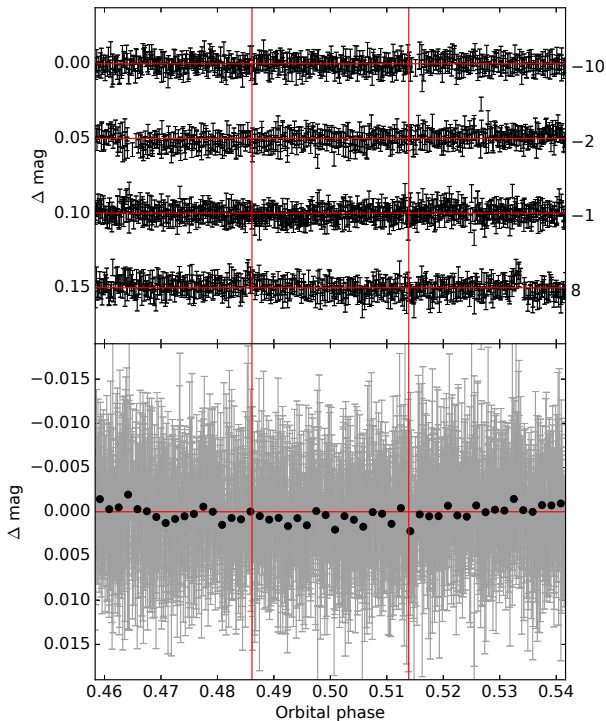


FIG. 5.— Secondary eclipse window for LP 261-75. Top panel: individual light curves with baseline flattened as Figure 3, with the secondary eclipse duration indicated by vertical red lines. Bottom panel: combined, phase-folded light curve, with bins as described for Figure 3. No secondary eclipse is detected.

radius ratio for each of the 8 primary eclipses to estimate the contribution of this source of error. The resulting unweighted mean of these radius ratios was found to be compatible with the joint solution given in Table 7 but the empirical error in the mean was 0.0012, or 0.00064 rejecting one outlier (the eclipse numbered 7 in Fig. 3). We therefore suggest the uncertainty reported for this parameter in the table may need to be inflated to account for the effect of the spot crossings.

We further note that the two velocities close to orbital phase 1.0 shown at the right-hand side of Figure 4 inadvertently overlapped the primary eclipse at the end of the exposures, so could be influenced by the Rossiter-McLaughlin effect. The resulting velocity anomaly would be approximately $+0.1 \text{ km s}^{-1}$ for these data points if the system is spin-orbit aligned. While they do show slightly elevated positive residuals compared to the model, we do not consider them to be significant at present. The Rossiter-McLaughlin effect has not been accounted for in modeling, and while the estimated observational uncertainties (via the s_1 parameter) are inflated by the presence of these residuals it is still possible some systematic errors exist in γ and K_1 and any parameters derived therefrom.

Since this is a single-lined spectroscopic binary, an estimate of the primary mass is needed to derive the properties of the secondary. LP 261-75 is a close kinematic match to the AB Dor moving group (e.g., Gagné et al. 2015), so we must first assess the age of the system in

order to determine which relations are appropriate for estimating the primary mass. Using our value for the γ velocity and the astrometric parameters in Table 1 we obtain $(U, V, W) = (-5.9 \pm 1.1, -28.7 \pm 1.3, -14.8 \pm 0.9) \text{ km s}^{-1}$. We quantify the kinematic match to AB Dor using the BANYAN Σ web tool (Gagné et al. 2018), obtaining a membership probability of 99%. However, there must also be independent observational evidence of youth before an object can be considered a moving group member, which we now proceed to examine.

This analysis is complicated by the structure of the AB Dor moving group. AB Dor “stream” stars do not appear to all have the same age and chemical composition, with the population likely consisting of a subsample of young stars which share a common origin with the main AB Dor “nucleus”, whereas the rest probably do not (e.g., Barenfeld et al. 2013). The age of the nucleus and young stream members of AB Dor is estimated to be 130–200 Myr in the recent work of Bell et al. (2015). Ages in this range have also been suggested to explain the observed properties of the M-dwarf primary in the present system, predominantly its high activity level (e.g., Reid & Walkowicz 2006; Shkolnik et al. 2009), but it is important to note that activity can be influenced by tides in close spectroscopic binaries, and we further find that strong $H\alpha$ activity and rotation periods of a few days may persist beyond 1 Gyr in some mid-M systems (e.g., Irwin et al. 2011a; Newton et al. 2016).

We do not find any clear observational evidence of youth in LP 261-75 at present. The position of the system on an M_G vs $G_{BP} - G_{RP}$ color-magnitude diagram (Figure 6) falls at the red end of the main locus of MEarth targets, which could simply result from high metallicity (e.g., Dittmann et al. 2016). The density of the primary is constrained from the light curve analysis, but is not strongly discriminating once we account for the known tendency of stellar models to underpredict the radii of field stars. The properties of the secondary are more sensitive to age, with evolutionary models (Chabrier et al. 2000; Baraffe et al. 2003) predicting the secondary would be approximately $0.14 - 0.15 R_\odot$ and sufficiently luminous to produce a secondary eclipse of several percent in MEarth if it was in the 100–200 Myr age range. The observed properties of the secondary and the lack of secondary eclipses are instead more consistent with the model predictions for Gyr ages.

Based on this argument, we conclude that the system is likely sufficiently old to apply relations for normal field stars to estimate the primary mass. We therefore use the K-band mass-luminosity relation (MLR) from Benedict et al. (2016) in conjunction with the 2MASS K-band magnitude and parallax from Table 1. We assume an uncertainty of 0.09 mag in absolute magnitude on the MLR, as stated in Table 12 of Benedict et al. (2016), and use the double-exponential form (absolute magnitude as a function of mass) which we find is better behaved at the extremes of the mass range than the polynomial relations. The parameters depending on the adopted MLR are indicated in Table 7.

7.4. LP 796-24

Figure 7 shows the light curve for this system. As discussed in §5, the spectroscopic quantities are not reliably measured, so we have not attempted a full solution

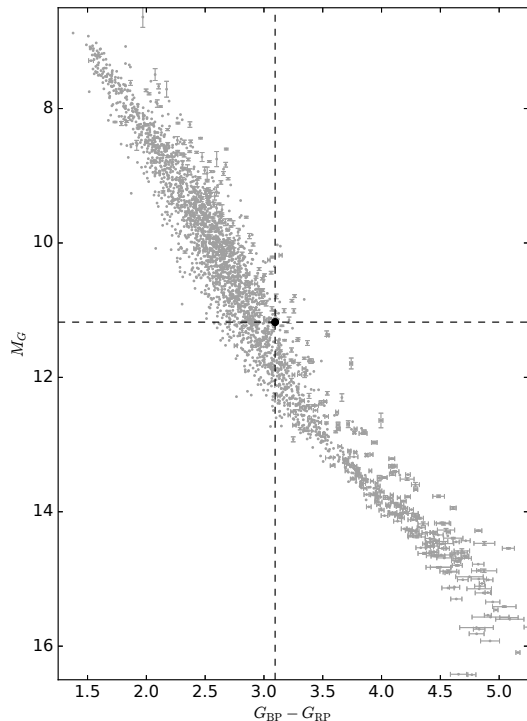


FIG. 6.— M_G versus $G_{BP} - G_{RP}$ color-magnitude diagram of the Nutzman & Charbonneau (2008) parent sample for MEarth-North, using the 2MASS cross-match table provided in GAIA DR2 to retrieve the GAIA data, and excluding known unresolved multiples. The criteria given in Gaia Collaboration et al. (2018b) were used to filter potentially contaminated G_{BP} and G_{RP} measurements based on the excess factor. LP 261-75 is plotted in solid black, and the position is indicated by the dashed lines.

and provide only the orbital ephemeris determined from the MEarth light curves in Table 2. Higher signal to noise ratio spectra, reliably detecting all three components, would be needed for a full analysis.

7.5. LP 991-15

Figure 8 shows the eclipse light curves for this system, and Figure 9 shows the out-of-eclipse modulation and the radial velocities. The orbital solution is given in Table 8.

Due to the lack of secondary eclipses, the light curve parameters in this system depend on the assumptions (in particular, the spectroscopic light ratio α and the adopted prior in the radius ratio) to a greater degree than is usual for double-lined eclipsing binaries with more normal configurations showing two eclipses. The surface brightness ratio parameter J , which is usually derived from the relative depths of the primary and secondary eclipses, is largely unconstrained by the data in this system, but it is still needed to interpret the observed primary eclipse depth to extract $\cos i$ and $(R_1 + R_2)/a$.

While the radius ratio is not determined, in theory the sum of the radii is still constrained by the observed eclipse duration. In practice, however, this inference also depends on other assumptions such as limb darkening parameters and third light to an extent which is not taken into account by the Monte Carlo procedure we have used to estimate uncertainties, and we do not attempt to pro-

TABLE 8
PARAMETERS AND UNCERTAINTIES FOR
LP 991-15.

Parameter	Value
Jump parameters	
J (see note)	0.93 ± 0.12
$(R_1 + R_2)/a$	0.01455 ± 0.00021
$\cos i$	0.01957 ± 0.00071
$e \cos \omega$	0.0136 ± 0.0011
$e \sin \omega$	0.51645 ± 0.00095
q	0.8489 ± 0.0024
F_1	0.86340 ± 0.00056
a_{11}	0.00622 ± 0.00031
b_{11}	0.00578 ± 0.00031
$(K_1 + K_2)$ (km/s)	57.605 ± 0.088
γ (km/s)	8.727 ± 0.026
C	1.042 ± 0.025
s_1 (km/s)	0.143 ± 0.020
s_2 (km/s)	0.277 ± 0.037
Derived parameters	
i (deg)	88.878 ± 0.041
e	0.51664 ± 0.00096
ω (deg)	88.49 ± 0.13
M_1 (M_\odot)	0.1969 ± 0.0011
M_2 (M_\odot)	0.16715 ± 0.00072

NOTE. — The value of J is determined by the combination of the priors on R_2/R_1 and L_2/L_1 and is not constrained observationally. We state it only for completeness.

vide or interpret this parameter given these difficulties. This system is therefore not currently useful to test the mass-radius relation. It is possible future highly precise light curves may be able to alleviate some of these degeneracies in models of the primary eclipse.

The component masses are well-determined, and while they depend on $\cos i$ from the light curve solution, the mere existence of primary eclipses is largely sufficient to constrain $\sin i$ for this purpose given the long orbital period. We caution that it is likely the uncertainties in the masses stated in Table 8 have been underestimated due to neglecting correlated noise in the radial velocity analysis, where the residuals in Figure 9 do appear to be correlated at a level approximately equal to the uncertainties, but we suspect they are indeed determined to better than 2%. Combined with the astrometric parallax, this system could therefore potentially be used to calibrate the mass-luminosity or absolute magnitude relations.

We thank Guillermo Torres and Eric Mamajek for discussing details of the solutions and the kinematics, respectively, and Todd Henry for encouragement to complete the CHIRON analysis. We also thank the staff at Fred Lawrence Whipple Observatory and Cerro Tololo Inter-American Observatory for assistance in the construction and operation of MEarth-North and MEarth-South; the CTIO 1.5m queue observers: Carlos Corco, Alberto Miranda, Leonardo Paredes, and Jacqueline Serón, for assistance with gathering the CHIRON observations; and the SMARTS queue managers: Emily MacPherson and Imran Hasan for assistance in planning, scheduling, and reducing the CHIRON observations. The MEarth team acknowledges funding from the David and Lucile Packard Fellowship for Science and

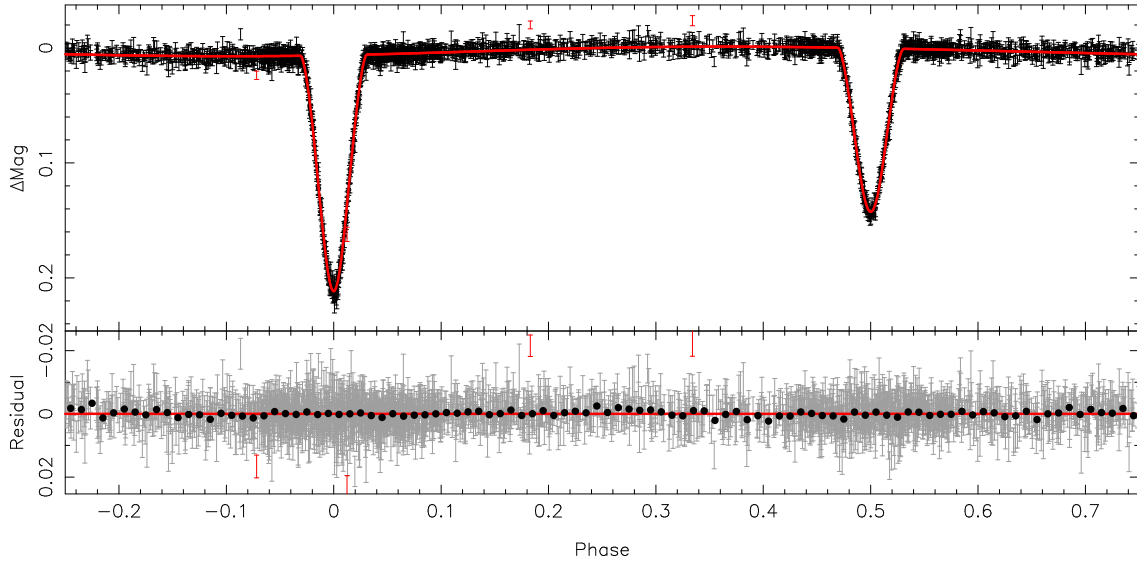


FIG. 7.— Phase-folded light curve for LP 796-24 with best fit overlaid. Panels are the same as described for Figure 2.

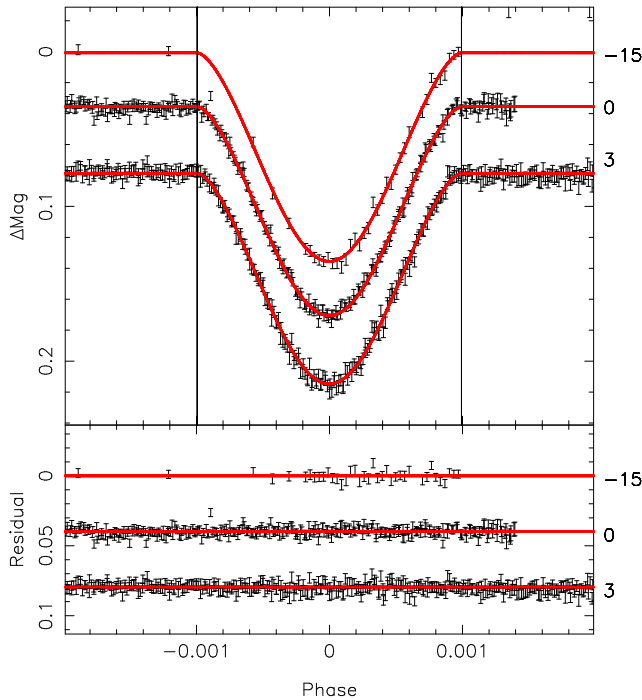


FIG. 8.— Primary eclipses for LP 991-15. Vertical offsets and light curve corrections are the same as described for Figure 3.

Engineering (awarded to D.C.). This material is based on work supported by the National Science Foundation under grants AST-0807690, AST-1109468, AST-1004488 (Alan T. Waterman Award) and AST-1616624. This publication was made possible through the support of a grant from the John Templeton Foundation. The opinions expressed in this publication are those of the authors and do not necessarily reflect the views of the John Templeton Foundation.

This research has made extensive use of data products from the Two Micron All Sky Survey, which is a joint project of the University of Massachusetts and the Infrared Processing and Analysis Center / California Institute of Technology, funded by NASA and the NSF, NASA’s Astrophysics Data System (ADS) bibliographic services, and the SIMBAD and VizieR databases, operated at CDS, Strasbourg, France. The Digitized Sky Surveys were produced at the Space Telescope Science Institute under U.S. Government grant NAG W-2166. The images of these surveys are based on photographic data obtained using the Oschin Schmidt Telescope on Palomar Mountain and the UK Schmidt Telescope. The plates were processed into the present compressed digital form with the permission of these institutions.

Facilities: CTIO:1.5m (CHIRON), FLWO:1.5m (TRES)

REFERENCES

- Altmann, M., Roeser, S., Demleitner, M., Bastian, U., & Schilbach, E. 2017, *A&A*, 600, L4, doi: 10.1051/0004-6361/201730393
- Andersen, J. 1991, *A&A Rev.*, 3, 91, doi: 10.1007/BF00873538
- Baraffe, I., Chabrier, G., Barman, T. S., Allard, F., & Hauschildt, P. H. 2003, *A&A*, 402, 701, doi: 10.1051/0004-6361:20030252
- Barenfeld, S. A., Bubar, E. J., Mamajek, E. E., & Young, P. A. 2013, *ApJ*, 766, 6, doi: 10.1088/0004-637X/766/1/6
- Bayless, A. J., & Orosz, J. A. 2006, *ApJ*, 651, 1155, doi: 10.1086/507981
- Bell, C. P. M., Mamajek, E. E., & Naylor, T. 2015, *MNRAS*, 454, 593, doi: 10.1093/mnras/stv1981
- Benedict, G. F., Henry, T. J., Franz, O. G., et al. 2016, *AJ*, 152, 141, doi: 10.3847/0004-6256/152/5/141
- Berta, Z. K., Irwin, J., Charbonneau, D., Burke, C. J., & Falco, E. E. 2012, *AJ*, 144, 145, doi: 10.1088/0004-6256/144/5/145
- Bryan, M. L., Bowler, B. P., Knutson, H. A., et al. 2016, *ApJ*, 827, 100, doi: 10.3847/0004-637X/827/2/100
- Buchhave, L. A., Bakos, G. Á., Hartman, J. D., et al. 2010, *ApJ*, 720, 1118, doi: 10.1088/0004-637X/720/2/1118
- Chabrier, G., & Baraffe, I. 1997, *A&A*, 327, 1039
- Chabrier, G., Baraffe, I., Allard, F., & Hauschildt, P. 2000, *ApJ*, 542, 464, doi: 10.1086/309513
- Claret, A., & Bloemen, S. 2011, *A&A*, 529, A75, doi: 10.1051/0004-6361/201116451
- Claret, A., Hauschildt, P. H., & Witte, S. 2012, *A&A*, 546, A14, doi: 10.1051/0004-6361/201219849

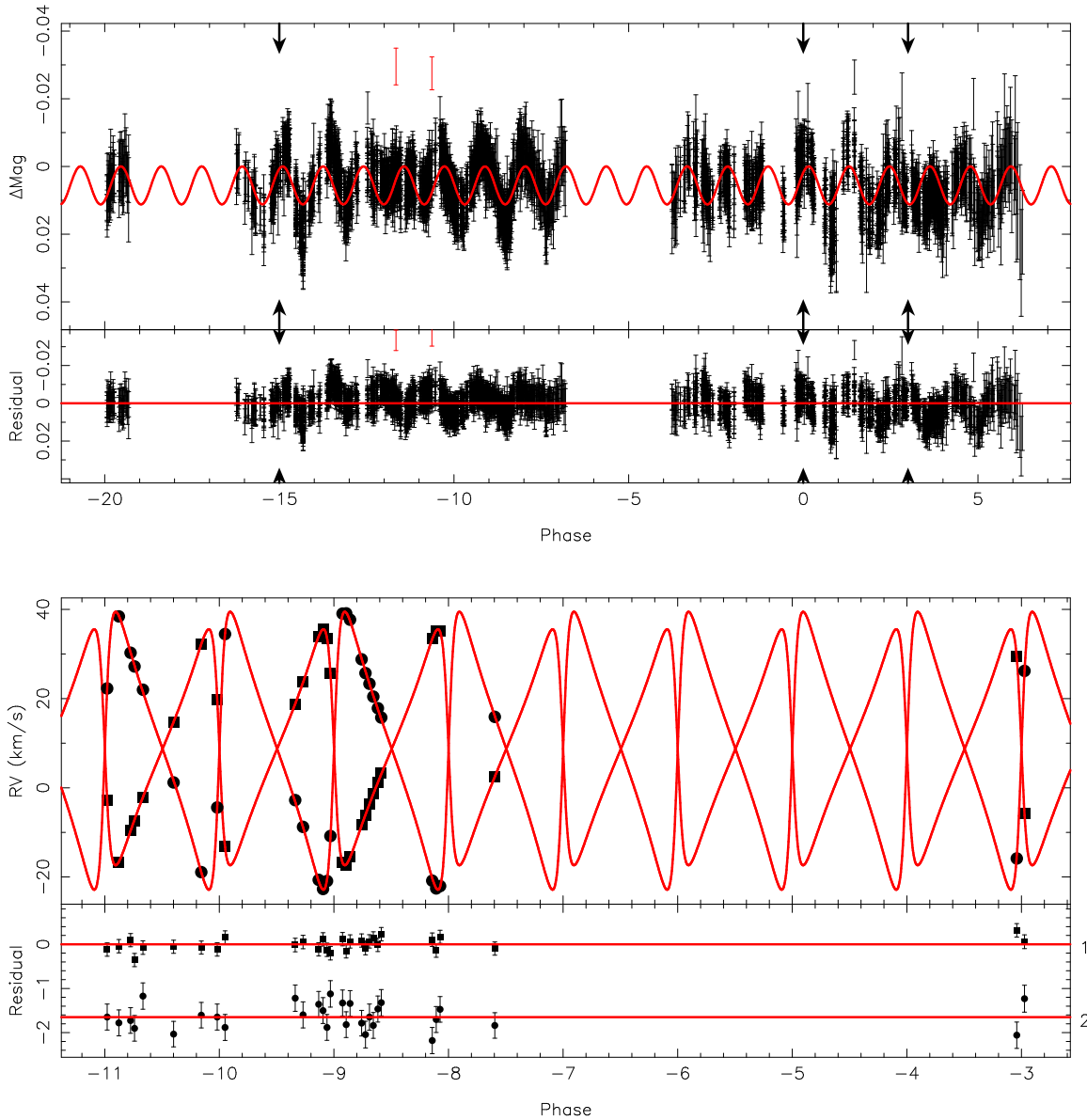


FIG. 9.— Top panels: out-of-eclipse light curve for LP 991-15, plotted as for Figure 3 with the observed primary eclipse epochs indicated by arrows. Bottom panels: radial velocity curve. Symbols and vertical offsets are the same as for Figure 2.

Dittmann, J. A., Irwin, J. M., Charbonneau, D., & Newton, E. R. 2016, *ApJ*, 818, 153, doi: 10.3847/0004-637X/818/2/153
Dittmann, J. A., Irwin, J. M., Charbonneau, D., et al. 2017, *ApJ*, 836, 124, doi: 10.3847/1538-4357/836/1/124
Donati, J.-F., Semel, M., Carter, B. D., Rees, D. E., & Collier Cameron, A. 1997, *MNRAS*, 291, 658, doi: 10.1093/mnras/291.4.658
Etzel, P. B. 1981, in *Photometric and Spectroscopic Binary Systems*, ed. E. B. Carling & Z. Kopal, 111
Foreman-Mackey, D., Hogg, D. W., Lang, D., & Goodman, J. 2013, *PASP*, 125, 306, doi: 10.1086/670067
Gagné, J., Faherty, J. K., Cruz, K. L., et al. 2015, *ApJS*, 219, 33, doi: 10.1088/0067-0049/219/2/33
Gagné, J., Mamajek, E. E., Malo, L., et al. 2018, *ApJ*, 856, 23, doi: 10.3847/1538-4357/aaae09
Gaia Collaboration, Brown, A. G. A., Vallenari, A., et al. 2018a, *ArXiv e-prints*. <https://arxiv.org/abs/1804.09365>
Gaia Collaboration, Babusiaux, C., van Leeuwen, F., et al. 2018b, *ArXiv e-prints*. <https://arxiv.org/abs/1804.09378>
Hambly, N. C., MacGillivray, H. T., Read, M. A., et al. 2001, *MNRAS*, 326, 1279, doi: 10.1111/j.1365-2966.2001.04660.x

Hoaglin, D. C., Mosteller, F., & Tukey, J. W. 1983, *Understanding robust and exploratory data analysis* (New York: Wiley)
Husser, T.-O., Wende-von Berg, S., Dreizler, S., et al. 2013, *A&A*, 553, A6, doi: 10.1051/0004-6361/201219058
Irwin, J., Berta, Z. K., Burke, C. J., et al. 2011a, *ApJ*, 727, 56, doi: 10.1088/0004-637X/727/1/56
Irwin, J., Charbonneau, D., Berta, Z. K., et al. 2009, *ApJ*, 701, 1436, doi: 10.1088/0004-637X/701/2/1436
Irwin, J., Buchhave, L., Berta, Z. K., et al. 2010, *ApJ*, 718, 1353, doi: 10.1088/0004-637X/718/2/1353
Irwin, J. M., Berta-Thompson, Z. K., Charbonneau, D., et al. 2015, in *Cambridge Workshop on Cool Stars, Stellar Systems, and the Sun*, Vol. 18, 18th Cambridge Workshop on Cool Stars, Stellar Systems, and the Sun, ed. G. T. van Belle & H. C. Harris, 767–772
Irwin, J. M., Quinn, S. N., Berta, Z. K., et al. 2011b, *ApJ*, 742, 123, doi: 10.1088/0004-637X/742/2/123
Kurtz, M. J., & Mink, D. J. 1998, *PASP*, 110, 934, doi: 10.1086/316207
Lépine, S. 2005, *AJ*, 130, 1680, doi: 10.1086/432792

- Lépine, S., & Shara, M. M. 2005, *AJ*, 129, 1483, doi: 10.1086/427854
- Mandel, K., & Agol, E. 2002, *ApJ*, 580, L171, doi: 10.1086/345520
- Markwardt, C. B. 2009, in *Astronomical Society of the Pacific Conference Series*, Vol. 411, *Astronomical Data Analysis Software and Systems XVIII*, ed. D. A. Bohlender, D. Durand, & P. Dowler, 251
- Nefs, S. V., Birkby, J. L., Snellen, I. A. G., et al. 2013, *MNRAS*, 431, 3240, doi: 10.1093/mnras/stt405
- Nelson, B., & Davis, W. D. 1972, *ApJ*, 174, 617, doi: 10.1086/151524
- Newton, E. R., Irwin, J., Charbonneau, D., et al. 2016, *ApJ*, 821, 93, doi: 10.3847/0004-637X/821/2/93
- Nutzman, P., & Charbonneau, D. 2008, *PASP*, 120, 317, doi: 10.1086/533420
- Parviainen, H., & Aigrain, S. 2015, *MNRAS*, 453, 3821, doi: 10.1093/mnras/stv1857
- Pecaut, M. J., & Mamajek, E. E. 2013, *ApJS*, 208, 9, doi: 10.1088/0067-0049/208/1/9
- Popper, D. M., & Etzel, P. B. 1981, *AJ*, 86, 102, doi: 10.1086/112862
- Reid, I. N., & Walkowicz, L. M. 2006, *PASP*, 118, 671, doi: 10.1086/503446
- Reid, I. N., Cruz, K. L., Allen, P., et al. 2003, *AJ*, 126, 3007, doi: 10.1086/379173
- Shkolnik, E., Liu, M. C., & Reid, I. N. 2009, *ApJ*, 699, 649, doi: 10.1088/0004-637X/699/1/649
- Skrutskie, M. F., Cutri, R. M., Stiening, R., et al. 2006, *AJ*, 131, 1163, doi: 10.1086/498708
- Southworth, J., Maxted, P. F. L., & Smalley, B. 2004a, *MNRAS*, 351, 1277, doi: 10.1111/j.1365-2966.2004.07871.x
- Southworth, J., Zucker, S., Maxted, P. F. L., & Smalley, B. 2004b, *MNRAS*, 355, 986, doi: 10.1111/j.1365-2966.2004.08389.x
- Tokovinin, A., Fischer, D. A., Bonati, M., et al. 2013, *PASP*, 125, 1336, doi: 10.1086/674012
- Torres, G., Andersen, J., & Giménez, A. 2010, *A&A Rev.*, 18, 67, doi: 10.1007/s00159-009-0025-1
- Torres, G., McGruder, C. D., Siverd, R. J., et al. 2017, *ApJ*, 836, 177, doi: 10.3847/1538-4357/836/2/177
- Winters, J. G., Irwin, J., Newton, E. R., et al. 2018, *AJ*, 155, 125, doi: 10.3847/1538-3881/aaaa65
- Zucker, S., & Mazeh, T. 1994, *ApJ*, 420, 806, doi: 10.1086/173605
- Zucker, S., Torres, G., & Mazeh, T. 1995, *ApJ*, 452, 863, doi: 10.1086/176354